Physical and mechanical depth relationships of rocks from the Rotokawa Geothermal Reservoir, Taupō Volcanic Zone, New Zealand

Marlène Villeneuve, Timothy P.C. Jones, Michael J Heap, Ben Kennedy, Jim Cole, Paul Siratovich

New Zealand Journal of Geology and Geophysics

ISSN: (Print) (Online) Journal homepage: www.tandfonline.com/journals/tnzg20

Physical and mechanical depth relationships of rocks from the Rotokawa Geothermal Reservoir, Taupō Volcanic Zone, New Zealand

Marlène C. Villeneuve, Timothy P.C. Jones, Michael J. Heap, Ben M. Kennedy, Jim W. Cole & Paul A. Siratovich

To cite this article: Marlène C. Villeneuve, Timothy P.C. Jones, Michael J. Heap, Ben M. Kennedy, Jim W. Cole & Paul A. Siratovich (14 Nov 2024): Physical and mechanical depth relationships of rocks from the Rotokawa Geothermal Reservoir, Taupō Volcanic Zone, New Zealand, New Zealand Journal of Geology and Geophysics, DOI: 10.1080/00288306.2024.2424847

To link to this article: https://doi.org/10.1080/00288306.2024.2424847

Published online: 14 Nov 2024.

NEW ZEALAND JOURNAL OF GEOLOGY AND GEOPHYSICS
https://doi.org/10.1080/00288306.2024.2424847

Taylor & Francis
Taylor & Francis Group

RESEARCH ARTICLE

OPEN ACCESS Check for updates

Physical and mechanical depth relationships of rocks from the Rotokawa Geothermal Reservoir, Taupō Volcanic Zone, New Zealand

Marlène C. Villeneuve [a], Timothy P.C. Jones [b]*, Michael J. Heap [c,d], Ben M. Kennedy [b], Jim W. Cole [b] and Paul A. Siratovich [b]*

[a]Subsurface Engineering, Montanuniversitat Leoben, Leoben, Austria; [b]School of Earth and Environment, University of Canterbury, Christchurch, New Zealand; [c]Universite de Strasbourg, CNRS, Institut Terre et Environnement de Strasbourg, UMR 7063, Strasbourg, France; [d]Institut Universitaire de France (IUF), Paris, France

ABSTRACT

The Rotokawa geothermal field is in the Taupō Volcanic Zone, New Zealand. It hosts two geothermal power plants, Rotokawa and Ngā Awa Pūrua, which together have a capacity over 170 MWe. The permeability of the rock mass comprising a geothermal field controls the volume of hot fluids that can be extracted for energy production. In this research we produce a stress model to estimate in-situ rock matrix permeability for a unique set of intact rock samples obtained from depths up to 2600 m in the Rotokawa geothermal field. We show that permeability generally decreases with sample depth, both intrinsically and in response to increasing confining pressure. We explore this confining pressure effect on other petrophysical and mechanical measurements, and highlight how rock texture and composition affect how the rocks respond to confining pressure. For example, we compare two altered andesite samples: a breccia with microfractures and infilled pores that tends to experience less compaction and porosity decrease than a lava with rounded, unfilled pores. We suggest that, when developing depth-models, measurements should be conducted at relevant in-situ conditions, if possible. Finally, we explore relationships between different physical parameters and provide estimating functions for those with the clearest correlations.

ARTICLE HISTORY
Received 2 July 2024
Accepted 18 October 2024

HANDLING EDITOR
Arishma Ram

KEYWORDS
Permeability; confining pressure; porosity; compaction; stress

Introduction

Permeability of reservoir rocks is a critical factor to the viability of a commercial geothermal field. In New Zealand, the geothermal fields are mainly located in the Taupō Volcanic Zone (TVZ), a very active volcanic region on the North Island with a remarkably high heat flux (4200 ± 500 MW; (Bibby et al. 1995; Hochstein 1995)). The TVZ has successfully been exploited for power generation since 1958, starting with the Wairakei Power Station. There are several fields that have been commercially developed for power generation in the TVZ, including the Rotokawa geothermal field, which is the study area of this research.

There are three factors controlling whether a geothermal resource is viable for exploitation; heat to provide initial energy, ground water to provide a mode of transport for this energy and a pathway for this heated fluid to flow, ultimately to the surface. The permeability of the rock mass comprising a geothermal system is dictated by the porosity and permeability of the intact component, or rock matrix, as well as its propensity to host permeability-enhancing fractures at all scales (e.g. McNamara et al. 2015; Heap and Kennedy 2016; Massiot et al. 2017; Heap et al. 2020). The physical and mechanical properties, such as matrix porosity and permeability, mechanical behaviour, and strength, of the intact component of the rock mass can vary significantly due to the influence of variable heat fluxes, dynamic fluid flow regimes and active tectonics present in geothermal systems (Davidson et al. 2012; McNamara et al. 2015). Combined, these factors produce commercial fields in the TVZ dominated by highly altered, fractured and micro-structurally complex rocks (Siratovich et al. 2014; Siratovich et al. 2016).

A major challenge for characterising the subsurface properties is the difficulty in obtaining measurements due to sparse coring in geothermal reservoirs. Developing relationships between parameters that can be measured without core samples, for example from wireline logs or cuttings, can be useful for estimating the parameters necessary for the optimisation and maintenance of geothermal resources. Investigating relationships between key chemical, physical and mechanical properties can be complicated (e.g.

CONTACT Marlène C. Villeneuve marlene.villeneuve@unileoben.ac.at
*Present address: Timothy P.C. Jones, T&G Global, Hawke's Bay, New Zealand; Paul A. Siratovich, Upflow, Taupō, New Zealand

Kereszturi et al. 2023). Cant et al. (2018) conducted a depth-analysis of physical properties of geothermal reservoir rocks for a unique sample set from core obtained during well drilling at the Ngā Tamariki geothermal field, which is located about 10 km north of the Rotokawa field. The objective of this work is to carry out a systematic physical and mechanical property study of another unique set of samples of intact rocks from the Rotokawa geothermal field, under laboratory conditions, to provide a similar depth-analysis, while also focussing on building relationships between properties that can only be measured in the laboratory and those that could be obtained from well logging and cuttings. Using the results of the laboratory testing, we have investigated the effect of microstructure and porosity on the matrix permeability and mechanical behaviour, explore potential relationships between the different parameters, for example how ultrasonic wave velocities relate to other parameters, determine the effect of increasing confining pressure on matrix permeability and develop a lithostatic model to generate depth profiles for the physical properties.

Geological setting

Rotokawa geothermal field (RGF)

The Rotokawa geothermal field (RGF) is situated in the central TVZ on the North Island of New Zealand and is approximately 10 km north-east of Taupō township (Figure 1a). The RGF is located within the Whakamaru Subdomain (Rowland and Sibson 2001) and on the boundary of the Whakamaru Caldera (Figure 1a). The TVZ has developed over the last ~2 Ma, and has become one of the most active regions of silicic volcanism in the world (Houghton et al. 1995). The volcanism is related to the active rifting arc/back-arc system, associated with the Hikurangi subduction trough where the Pacific Plate descends underneath the Australia plate (Cole et al. 2014). There are 23 geothermal systems, including 17 high temperature systems (>250 °C) within the greater TVZ area (Bibby et al. 1995) (Figure 1).

Rock types at and near the surface of the RGF include rhyolite intrusives, lavas and pyroclastics, pumice alluvium, Wairakei breccia and hydrothermal eruption breccias (Rae 2007; McNamara et al. 2016;

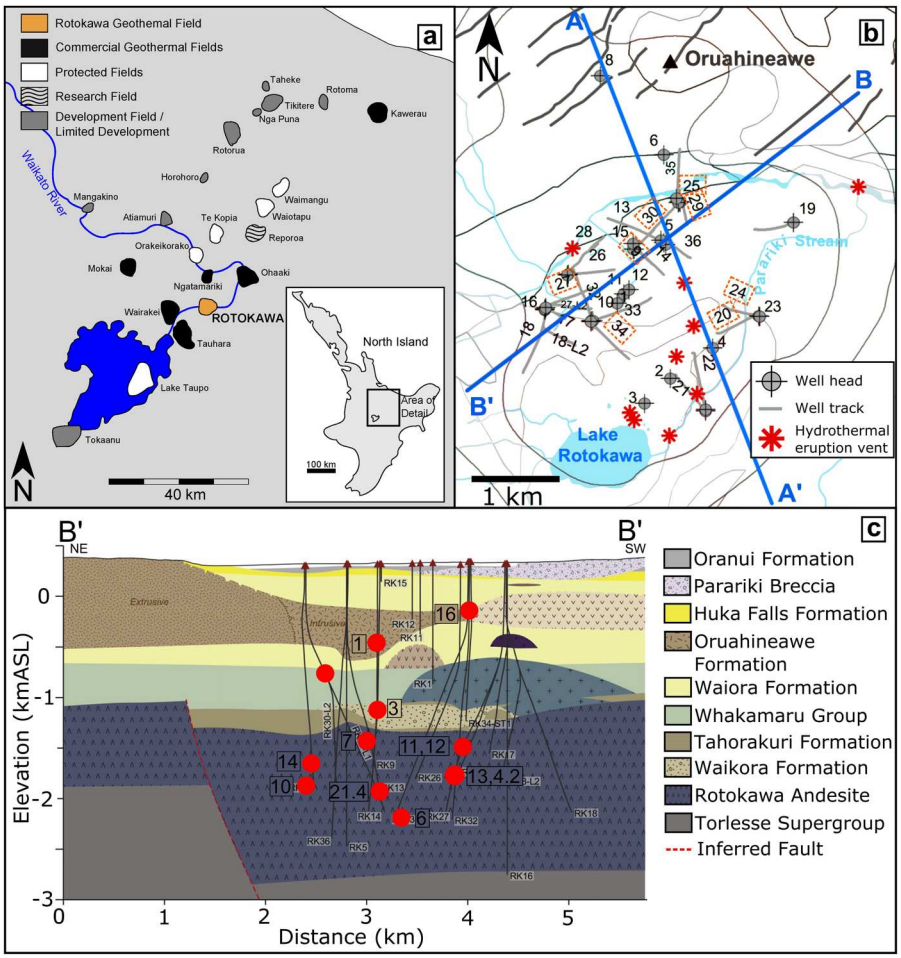

Figure 1. a) Location of Rotokawa geothermal field relative to other geothermal fields in the Taupō Volcanic Zone; modified from (Siratovich et al. 2014) with added Whakamaru Caldera boundary based on (Brown et al. 1998). b) Wells of the Rotokawa geothermal field; modified from (Milicich et al. 2020). Wells highlighted with red dashed boxes are the source of core used in this study. c) Simplified cross section through the Rotokawa geothermal field showing approximate depths and stratigraphic units from which the samples were taken; modified from Milicich et al. (2020); legend only contains units from Table 2.

Montanaro et al. 2023). The subsurface geology is complex and is the result of regionally extensive northeast trending faulting followed by post basement volcano-stratigraphic sequences from andesite and rhyolitic volcanic complexes (Rae 2007). A full description of the RGF subsurface geology has been given in McNamara et al. (2016) and references therein.

Methods and materials

Sample preparation and testing was carried out on sections of core supplied by the Rotokawa Joint Venture (Mercury Limited & Tauhara North No.2 Trust) from their Rotokawa core shed. The core pieces were from eight wells across the field (RK09, RK20, RK24ST1, RK25, RK27, RK29, RK30 and RK34) and from various depths (501 m to 2606 m below the local drilling relative level; Figure 1b,c). This ensured the data collected were from varying lithological units across the field. Table 1 provides a numbered system for each prepared sample set, along with well number, depth and rock type. Testing and preparation were carried out at the University of Canterbury (UC) School of Earth and Environment (New Zealand) unless otherwise stated. The samples were drilled to 20 mm in diameter and cut and precision-ground to as close to 40 mm in length as possible (i.e. twice their diameter). Samples were all drilled parallel to the core long axis. Following their preparation, all samples were washed and dried. A set of four individual samples were drilled from each well and depth; a total of 44 samples.

Table 1. Depth and well information for each sample set provided by the Rotokawa Joint Venture with associated stratigraphic units and sample set numbers. Stratigraphic units are according to Milicich et al. (2020).

Sample set	Depth (m)	Well #	Rock type	Stratigraphic Unit
16	501	RK34	Rhyolite breccia	Oruahineawe Rhyolite
1	905	RK09	Rhyolite lava	Oruahineawe Rhyolite
15	1113	RK30	Rhyolite pumice ignimbrite	Whakamaru Ignimbrite
3	1511	RK09	Fine-grained sandstone conglomerate	Waikora Formation
7	1821	RK24ST1	Brecciated andesite	Rotokawa Andesite
11	1852	RK27	Andesite breccia	Rotokawa Andesite
12	1854	RK27	Andesite lava clast	Rotokawa Andesite
14	2081	RK29	Andesite lava	Rotokawa Andesite
4.2	2121	RK27	Andesite lava	Rotokawa Andesite
13	2147	RK27	Andesite lava	Rotokawa Andesite
10	2200	RK25	Andesite breccia	Rotokawa Andesite
21.4	2320	RK30	Andesite breccia	Rotokawa Andesite
6	2606	RK20	Fine grained sandstone	Torlesse Supergroup

Thin section interpretation

Thin section interpretation was carried out on 13 polished thin sections, one to represent each sample set. Thin sections were examined to highlight key minerals, textures and alteration. Key minerals identified from each thin section can be found in the supplementary data. Each thin section was categorised by level of alteration: none, minor, moderate or high. These categories were selected in accordance with the similar detailed thin section descriptions in the GNS Science reports (Rosenberg 1997; Milicich et al. 2008; Rae et al. 2009; Ramirez and Rae 2009; Rae et al. 2010; Sanders et al. 2015).

Each thin section was carbon coated for analysis using a JEOL JSM-7000F Field Emission Scanning Electron Microscope (SEM) in the Mechanical Engineering Department (UC). Rather than calculating quantitative values for thin section porosity and fracture density (as in Cant et al. (2018) and Siratovich et al. (2014)), qualitative descriptions of the SEM images are used to help indicate relationships with texture.

Lithostatic stress model

Many studies assume a constant rock density of 2500 kg/m^3 for their lithostatic models and ignore fluid densities (e.g. White and Mroczek 1998; Sibson and Rowland 2003). To improve on this a lithological effective vertical (lithostatic) stress model was developed in order to estimate the in-situ effective confining pressure applied to each sample set in the reservoir. The method for developing the model was similar to that used in Cant et al. (2018), although we also considered the changes in rock and water density with increasing temperature and depth. Thickness and sequence of the rock units for each of the eight wells were collated from the well logs produced by GNS Science (Rosenberg 1997; Milicich et al. 2008; Rae et al. 2009; Ramirez and Rae 2009; Rae et al. 2010; Sanders et al. 2015). Estimates of dry densities were either averaged from those calculated in this research or obtained from the literature (Table 2).

Water density decreases with increasing temperature. For each rock unit, an average water temperature was calculated using temperature logs supplied by Mercury Ltd. When in aqueous phase, pressure has little effect on the density of water (i.e. it is incompressible) and is not accounted for in Equation 1.

$$\rho_w = 1000\left[1 - \frac{T + 288.9144}{508929.2(T + 68.12963)}(T - 3.9863)^2\right] \quad (1)$$

Where ρ_w = density of water (kg/m^3) and T = temperature (°C). The two end member densities at 4 and 350° C are, respectively, 1000 and 640 kg/m^3, showing that the effect of increasing temperature within this range

Table 2. Rock density information.

Stratigraphic unit	Rock type	Source	Dry Density (g/cm^3)
Oruanui Formation	Pumice tuff and rhyolite lava	Palmer (1982)[b]	1450
Parariki Breccia	Tuffaceous hydrothermal breccia	Montanaro et al. (2023)	2100
Huka Falls Formation	Siltstone and sandstone	Oetomo (2015)[a]	1033
Huka Falls Formation	Tuff siltstone	Wohletz and Heiken (1992)[c]	2000
Oruahineawe Formation	Rhyolite lava and breccia	This research	2201
Waiora Formation	Tuff	Oetomo (2015)[a]	2140
Whakamaru Ignimbrite	Ignimbrite	This research	1913
Tahorakuri Formation	Lithic tuff volcaniclastics	(Wyering et al. 2014; Cant et al. 2018)[a]	2360
Waikora Formation	Greywacke conglomerate	This research	2509
Rotokawa Andesite	Andesite breccia	This research	2481
Rotokawa Andesite	Andesite lava & breccia	This research	2496
Rotokawa Andesite	Andesite lava	This research	2510
Torlesse Supergroup	Basement greywacke	This research	2509

[a]Density estimate is from the TVZ but not from Rotokawa.
[b]Density estimate is from a similar rock description outside TVZ.
[c]Density estimated from a standard rock description. Stratigraphic unit names are according to Milicich et al. (2020).

results in a 35% density reduction. Increasing temperature also reduces rock dry density, however, for temperatures less than 400°C, (Zhu et al. 2022) showed that the dry density decrease is less than 1%. The porosity was used to calculate a saturated density using the proportion of solids and water, and their corresponding densities. For the density of the solids, we used a grain density ranging between 2250 and 2800 kg/m^3, and for the water we used Equation 1.

Using Equations 2, 3 and 4, the estimated total and effective lithostatic stresses were calculated for each unit and well. The cumulative stress was used to generate a stress model for each sample set.

$$\sigma = \rho_l g h \tag{2}$$

$$\sigma' = \sigma - u \tag{3}$$

$$u = \rho_w g h \tag{4}$$

Where σ' = effective stress (MPa), σ = lithostatic stress (kg/m^3), ρ_l = density of lithological unit (kg/m^3), u = pore pressure (MPa), ρ_w = density of water (kg/m^3), g = gravitational acceleration (m/s^2), and h = depth of interest (m).

There are many possible formulations for developing a lithostatic stress model. We selected different rock density (dry, saturated, constant, variable), water temperature (variable, constant at 4 °C), and pore pressure conditions to compute eight lithostatic stress models, described in Table 3.

Table 3. Lithostatic stress model descriptions.

Model name	Model description
Total Stress (constant density 2500 kg/m^3)	conventional, total stress model with constant dry rock density of 2500 kg/m^3
Total Stress (variable density)	total stress model with dry rock density integrated over unit thickness
Total Stress (saturated)	total stress model with saturated rock density integrated over unit thickness
Total Stress (temperature)	total stress model with variable dry rock density, decreased by 1% to account for high temperature
Total Stress (pressure)	a total stress model with variable dry rock density, increased by 1% to account for high pressure
Effective Stress (4 degrees)	effective stress model with variable dry rock density and density of water at 4 °C
Effective Stress (temperature)	effective stress model with variable dry rock density and density of water corresponding to the increasing temperature
Effective Stress (temperature, saturated)	effective stress model with variable saturated rock density and density of water corresponding to the increasing temperature

Several assumptions are made for these lithostatic models: 1. Each unit is considered homogeneous, but can show slight variation. 2. Averaged densities for each unit were used. 3. The hydrostatic component assumes a continuous linked aquifer and the entire system is 'wet' with no gas present and each unit is at the same temperature throughout. 4. The density calculations assume pure water rather than brine. 5. The water is assumed to be incompressible. 6. The rock density decrease with temperature (~2% over the considered range) is assumed to be offset by the density increase with depth (less than 3% over the considered range).

Petrophysical characterisation

Porosity and density

The International Society for Rock Mechanics (ISRM) standard for the saturation and buoyancy technique was used to determine the connected porosity (henceforth called porosity) and bulk dry density (henceforth called density) of each sample (Ulusay and Hudson 2007). Sample sets 1, 11, 15, and 16 (see Table 1) had swelling clays present. For these samples, gas pycnometry was performed using an Ultrapycnometer 1000 by Quantachrome Instruments at the University of Waikato (New Zealand) to determine their skeletal volume. Dry bulk density for these samples was determined using the ISRM standard for the calliper technique. The connected porosity for these samples was then determined using the skeletal volume from the pycnometer and the bulk volume from the calliper technique.

Permeametry

Permeability testing was carried out on a PDP-200 Pulse Decay Permeameter in the Engineering Geology

Laboratory (UC), previously described in (Cant et al. 2018; Mordensky et al. 2018). The PDP-200 has the ability to biaxially confine samples up to 60 MPa, as a proxy for lithostatic confining pressure. Permeability was measured on dry samples using gas as the pore fluid. Most samples were tested at confining pressures from 5 to 30 MPa, increasing by 5 MPa between each permeability measurement. For samples obtained from shallow depth, where the confining pressure is low, samples were only tested up to 15 MPa. A Klinkenberg correction was applied to all results. Samples that were too permeable for the instrument (permeability greater than 5×10^{-16} m^2) were not measured. Samples with very low-permeability were only tested up to 20 MPa (at which point permeability was less than 1×10^{-18} m^2). All measurements were performed at ambient laboratory temperatures.

Ultrasonic wave velocities

Ultrasonic wave velocity (v_p and v_s) measurements were carried out on each sample using a Computer Aided Ultrasonic Velocity Testing System (CATS ULT-100) manufactured by Geotechnical Consulting and Testing Systems (GCTS), as described in Mordensky et al. (2018). Measurements were performed on dry samples at ambient laboratory temperatures. Ultrasonic wave velocities were determined along the long axis of the cylindrical core samples. Ultrasonic wave velocities were used to determine dynamic Young's modulus and dynamic Poisson's ratio.

Mechanical testing

Triaxial compression testing was carried out on two samples from sample sets 11 and 14 at the Strasbourg Institute of Earth & Environment (France) (see schematic diagram in Farquharson et al. (2017)). Water-saturated (deionised water) samples were deformed under triaxial conditions (i.e. $s_1 > s_2 = s_3$) at a constant displacement rate corresponding to a constant strain rate of 10^{-5} s^{-1}. For all experiments, the pore fluid (deionised water) pressure was kept constant at 10 MPa, and experiments were performed at a confining pressure of either 50 or 80 MPa (i.e. effective pressures of 40 and 70 MPa, respectively, assuming a simple effective pressure law). All experiments were performed at ambient laboratory temperatures. Pore fluid and confining pressures were kept constant during the experiment using high-pressure pumps. Axial displacement was measured using an external linear variable differential transducer, and axial force axial load was measured using the oil pressure inside a pressurised chamber above the pressure vessel, the chamber diameter, and the diameter of the piston. Axial displacement and force were converted to strain and stress using the sample dimensions. Pore volume change (i.e. the change in sample porosity) was also calculated using data from the pore pressure encoder attached to the pore fluid pressure pump.

Results

Lithostatic stress model

Figure 2 provides a comparison of the eight different effective and total stress models for well RK 25. The conventional total stress model based on constant dry rock density provides the highest lithostatic stresses at all depths. The three total stress models based on variable dry rock density have similar lithostatic stresses, arising from the modest 1% increase or decrease of dry rock density for each model. The total stress model based on variable saturated rock density results in lithostatic stresses up to 5 MPa higher than those from the other total stress models at reservoir depth (~2000m). The effective stresses are up to 20–25 MPa lower than the total stresses at reservoir depth. The effective stress using variable water density according to temperature is up to 5 MPa higher than the effective stress using constant water density at reservoir depth. The differences in effective stress when considering dry or saturated density are less than 5 MPa. Considering the significant additional effort and uncertainty associated with calculating the saturated density, we consider the effective stress model with variable dry rock density and variable water density according to temperature (model 7,

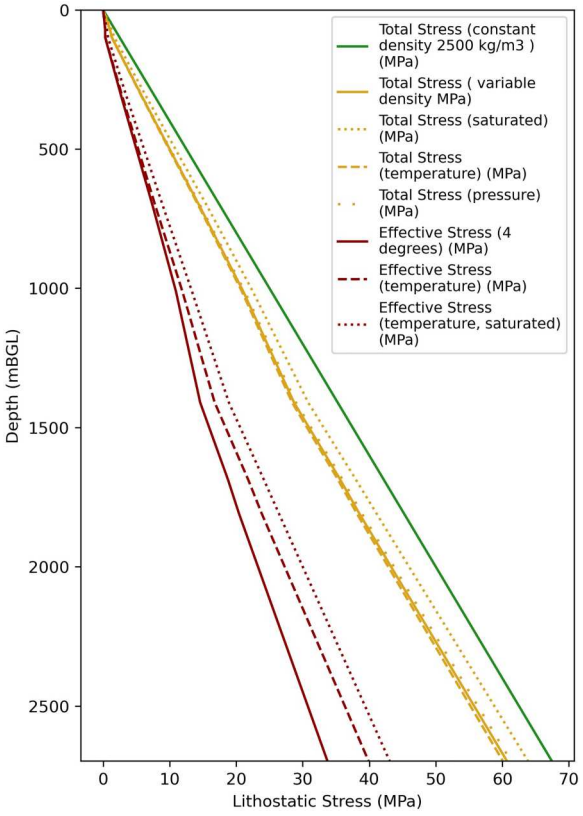

Figure 2. Lithostatic stress models of RK25 using different formulations; mBGL = meters below ground level.

'Effective Stress (temperature)') to be sufficiently representative of the in-situ effective vertical stress.

Petrophysical characterisation

The results of the petrophysical characterisation are summarised in Table 4. The full dataset is provided in the supplemental data and, when plotted in a scatter matrix, shows that many parameters correlate to each other (Figure 3). The diagonal showing the dataset distributions also highlight that the data are not all normally distributed, and in particular, porosity, density and permeability in this dataset may not be suitable for statistical analysis. The quality of the correlations between the parameters are given in a correlation matrix (Figure 4), which shows the Pearson's R (strength and direction of a linear relationship) as a heat map (where red represents positive relationships, blue represents negative relationships and white represents no relationship). The coefficient of

Table 4. Average porosity, density, ultrasonic wave velocity, dynamic Poisson's ratio and dynamic Young's modulus (refer to Table 1 for sample set descriptions; refer to supplemental data for full dataset).

Sample set	Permeability at 5 MPa confining pressure (m)	Porosity (%)	Dry Bulk Density (g/cm^3)	*P*-wave velocity (m/s)	S-wave velocity (m/s)	Dynamic Poisson's ratio	Dynamic Young's modulus (GPa)
16	2.46E-18	10	2.01	4024	2143	0.3	23.6
1	2.46E-18	10	2.38	4722	2529	0.3	38.9
15	-	25	1.91	2682	1573	0.24	11.7
3	1.16E-18	10	2.51	4774	2347	0.34	37.1
7	9.15E-19	9	2.58	4489	2476	0.28	40.4
11	6.93E-18	16	2.33	4101	2679	0.13	37.7
12	5.33E-18	16	2.36	4387	2201	0.33	30.4
14	2.24E-16	17	2.27	4225	2384	0.27	32.8
27_4.2	3.75E-19	6	2.59	4443	2603	0.24	43.5
13	-	2	2.80	4533	2553	0.27	46.4
10	5.39E-18	13	2.42	4545	2428	0.3	37.2
30_21.4	6.46E-19	7	2.58	4054	2514	0.19	38.7
6	3.84E-19	4	2.68	4878	2709	0.28	50.3

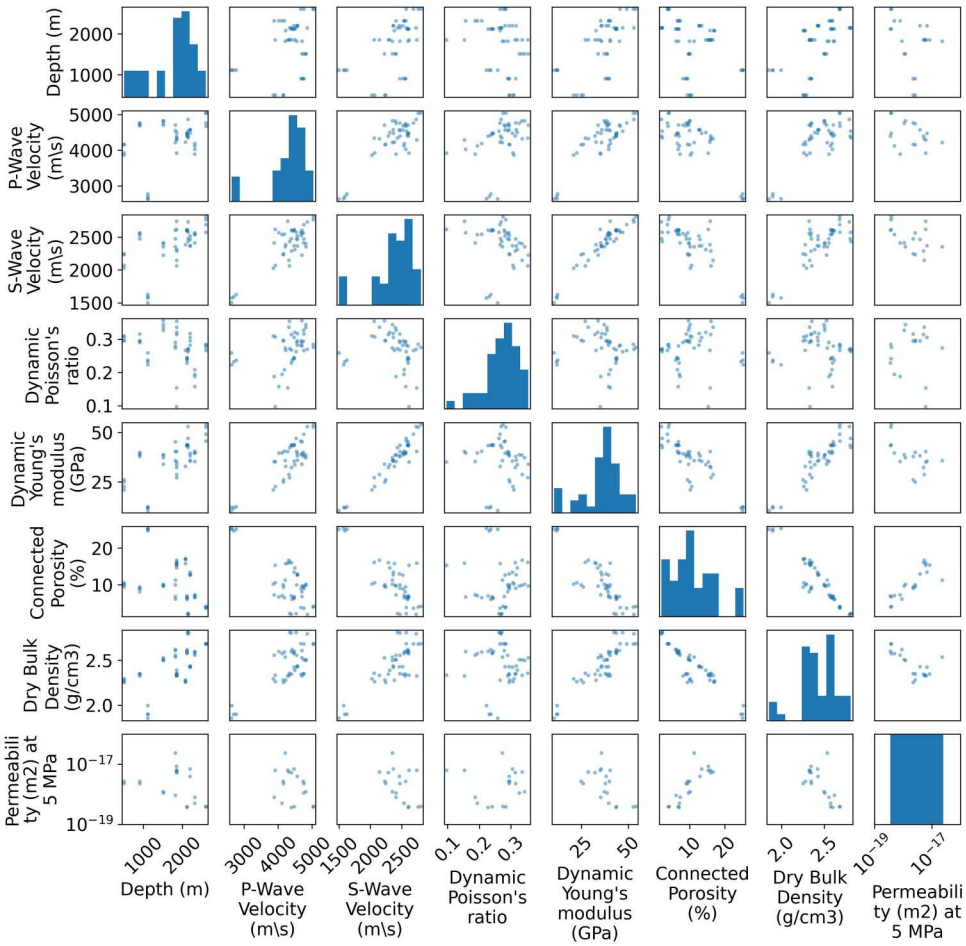

Figure 3. Scatter matrix of petrophysical characterisation results. Diagonal shows univariate distribution of each petrophysical characteristic as a histogram, which provides insights into the spread and concentration of the measurements. The y-axis for each plot differs according to the number of values.

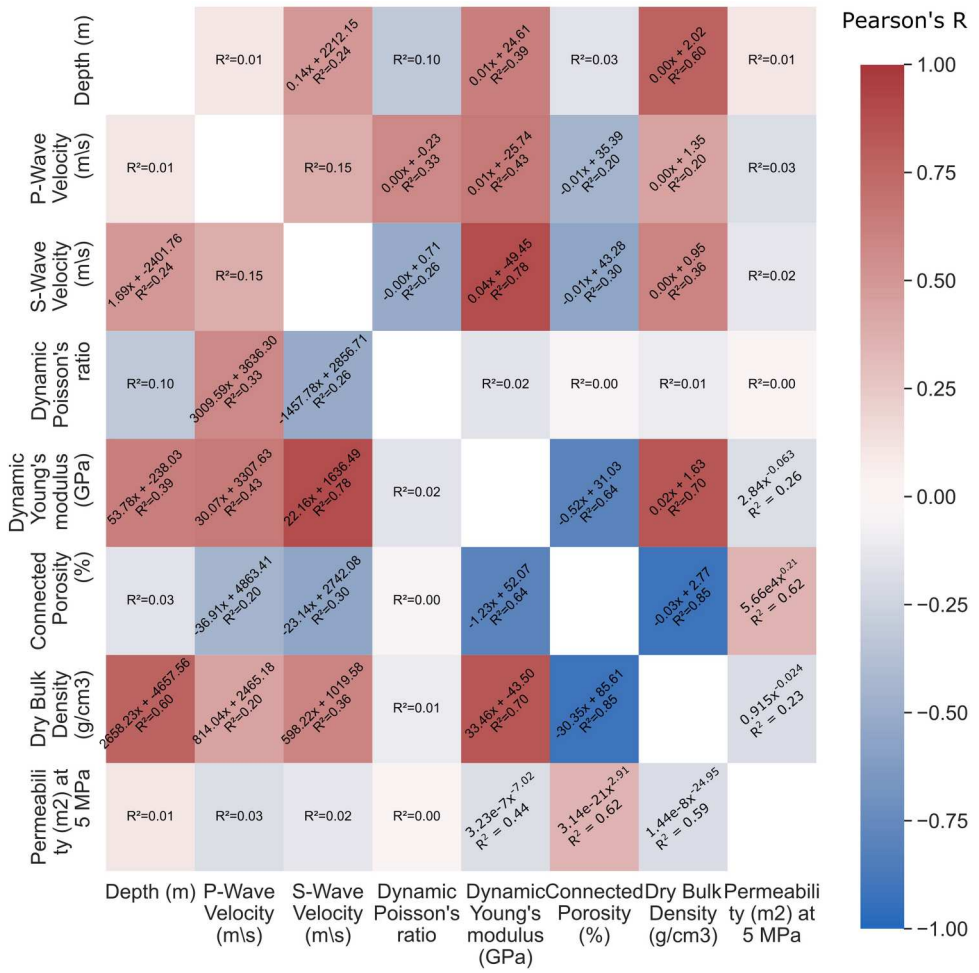

Figure 4. Correlation matrix showing Pearson's R as a heatmap and corresponding coefficient of determination R^2 for a linear regression, except for permeability, for which the R^2 is for a power model. For the parameters with Pearson's R > 0.4, the linear regression itself is also given. For the permeability, a power regression is given for the three best fits; note that the R^2 values are for the linear regression on the log-transformed data used to derive the power function.

determination, R^2, is also given, as text. For all datasets except for permeability, the R^2 refers to a linear regression (derived using the scipy stats function linregress), whereas for permeability it refers to a fit to a power model (derived using the sklearn linear model function Linear Regression for a log-transformed power model; note the R^2 values are for the linear regression on the log-transformed data used to derive the power function). For the datasets with R > 0.4, the linear regression is also given. For the permeability, the three best power models are given. The datasets that show the best or most interesting correlations are plotted and discussed in more detail in the relevant subsections.

Porosity and density

The porosity and density of the samples range between 2–25% and 1.9–2.8 g/cm^3, respectively. The relationship in Figure 5 follows what has also been demonstrated for TVZ rocks (Siratovich et al. 2014; Wyering et al. 2014; Cant et al. 2018; Mordensky et al. 2018; Schaefer et al. 2023), as well as for other

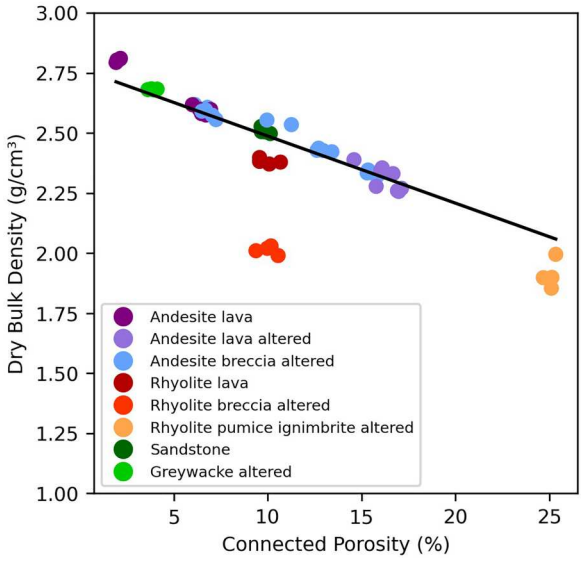

Figure 5. Porosity versus density, colour coded according to lithological description; see Figure 4 for the equation for the linear regression (regression excludes data for the altered rhyolite breccia).

volcanic rocks, e.g. Massiot et al. (2022) (Brothers volcano, a Pacific Ocean submarine volcano in the Kermadec Arc, 340 kilometres northeast Whakaari volcano at the northernmost end of the TVZ) and Heap et al. (2014) (Volcán de Colima, Mexico): the bulk dry density decreases systematically with increasing porosity. Our proposed linear relationship is also consistent with those provided in Wyering et al. (2014); Cant et al. (2018); and Massiot et al. (2022). The altered rhyolite breccia appears to have isolated porosity that is not captured by the connected porosity measurement, such that it does not fall on the trend. This may be associated with partially recrystallised pumice clasts with locally isolated pores within the breccia. As a result, for deriving the fitting relationships (permeability-density, permeability-Young's modulus, porosity-density, porosity-wave velocities and the porosity-elastic moduli) in Figure 4, the data for the rhyolite breccia altered have been excluded.

Permeametry

Permeability at confining pressure of 5 MPa ranges from 3.64×10^{-19}–8.4×10^{-18} m^2. Permeability increases as a function of porosity, but decreases as a function of density and dynamic Young's modulus (Figure 6). These data highlight a clear power relationship between porosity and permeability (Figure 6a), as previously shown for volcanic rocks from the TVZ (e.g. Mordensky et al. 2018) and elsewhere (e.g. (Farquharson et al. 2015; Colombier et al. 2017; Rossetti et al. 2019)). We also find a that a power model can be fit to the density and permeability data if the data for the rhyolite breccia altered are removed (Figure 6b). Contrary to Siratovich et al. (2015), we find no relationship between P-wave or S-wave velocity and permeability (Figure 3), likely because the range of ultrasonic wave values in our dataset is too small for the wide range of permeabilities to result in a meaningful relationship with Pearson's R greater than 0.4, however, there is a weak relationship between dynamic Young's modulus and permeability, again with the data for the rhyolite breccia altered removed (Figure 6c), likely because density is used in the calculation of dynamic Young's modulus.

The effect of confining pressure on permeability varies from minimal to up to one order of magnitude over the tested range (Figure 7) (as also shown in Vinciguerra et al. 2005; Fortin et al. 2011; Nara et al. 2011; Cant et al. 2018; Heap et al. 2022). The largest decreases in permeability as a function of confining pressure are seen in the low-permeability sample sets (Figure 7). Sample set 6, for example, decreases from an average permeability of 3.48×10^{-19} to 7.15×10^{-20} m^2 as confining pressure is increased from 5 to 20 MPa. For the sample set with the highest permeability, sample set 14, permeability does not change appreciably (average permeability decreases from 2.23×10^{-16} to 2.15×10^{-16} m^2) as confining pressure is increased from 5 to 30 MPa (Figure 7). The full permeability dataset is given in the supplementary material.

Ultrasonic wave velocities

Key relationships with ultrasonic wave velocities and dynamic Young's modulus are porosity (Figure 8), density (Figure 9) and permeability (Figure 6c), as also highlighted for other volcanic rocks from New Zealand (Durán et al. 2019; Rossetti et al. 2019; Kanakiya et al. 2022; Massiot et al. 2022; Schaefer et al. 2023). P – and S-wave velocities decrease from 5043 m/s to 2629 m/s and from 2808 m/s to 1500 m/s, respectively, when porosity increases from 2 to 25% and density decreases from 2.8 to 1.8 g/cm^3 (Figure 8a and Figure 9a). Similarly, dynamic Young's modulus decreases from 53.9 to 10.5 GPa over the same porosity and density ranges (Figure 8b and Figure 9b).

Thin section interpretation

Thin section images from the petrographic microscope can be found in the supplemental material. Five thin sections were additionally examined with the SEM for more detailed microstructural analysis:

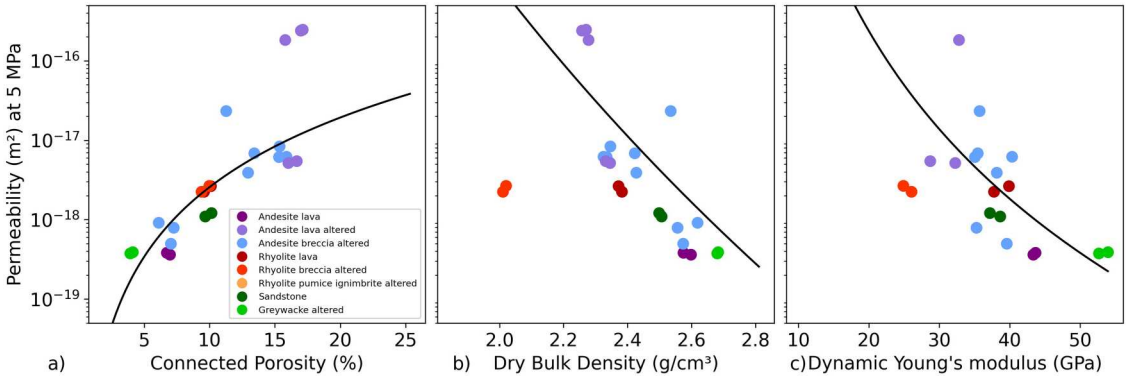

Figure 6. Permeability versus a) porosity, b) density and c) dynamic Young's modulus, colour coded according to lithological description; see Figure 4 for the equations for the power models (regressions for density and dynamic Young's modulus exclude data for the altered rhyolite breccia).

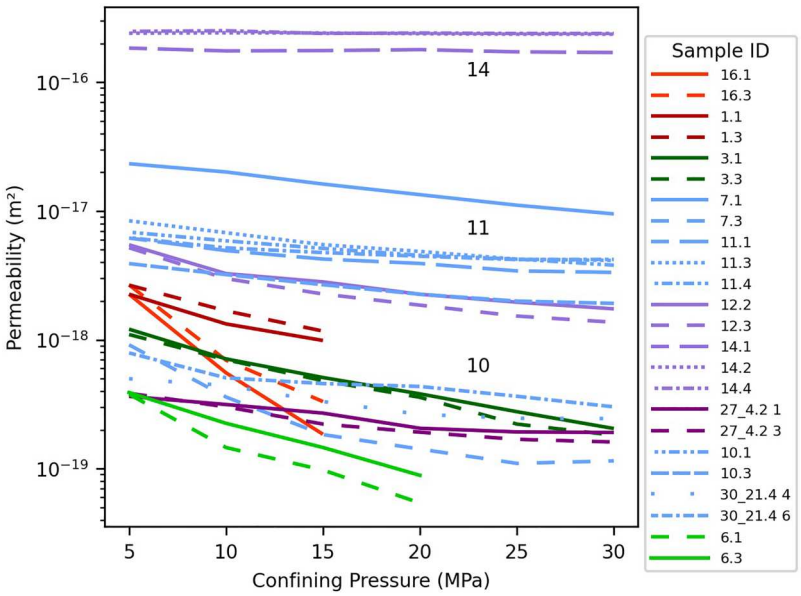

Figure 7. Permeability plotted against confining pressure for each sample. Labels in legend are in order of increasing depth and colour coded according to rock type as in Figure 5. Numerals in plot help locate the plots for sample sets 14, 11 and 10.

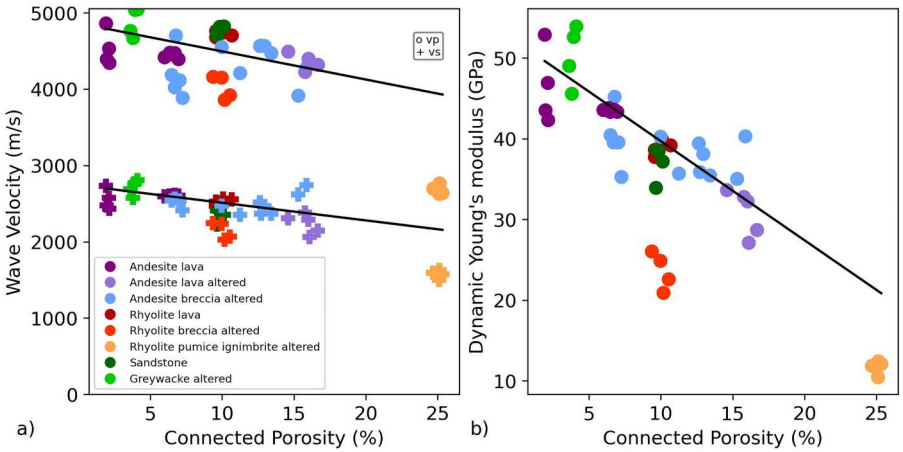

Figure 8. Porosity plotted against a) ultrasonic wave velocities and b) dynamic Young's modulus, colour coded according to lithological description; see Figure 4 for the equations for the linear regressions (regressions exclude data for the altered rhyolite breccia).

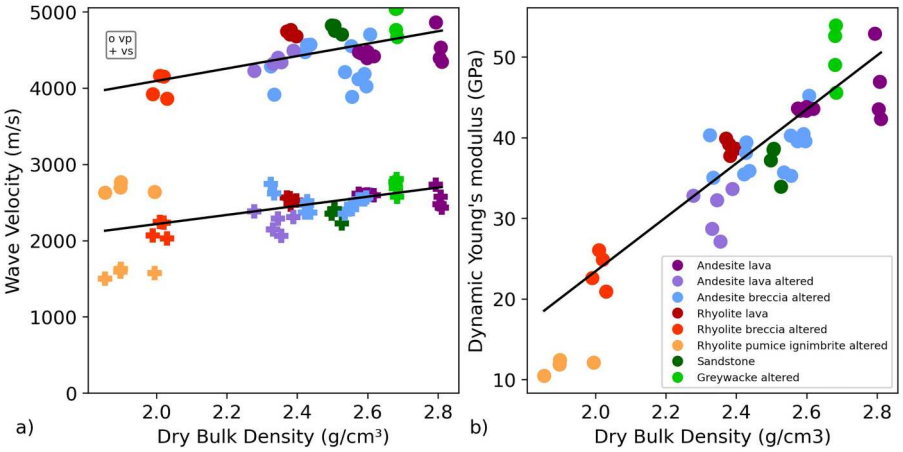

Figure 9. Density plotted against ultrasonic a) wave velocities and b) dynamic Young's Modulus, colour coded according to lithological description; see Figure 4 for the equations for the linear regressions.

1 (rhyolite lava), 6 (basement greywacke), 10 (andesite breccia), 11 (andesite breccia) and 14 (andesite lava). Figure 10 highlights the textural differences between samples 11 and 14 visible in the SEM images. In thin section 11 (Figure 10 left: altered andesite breccia), the pores in the rock are connected by microfractures, which propagate through phenocrysts, but do not propagate through the groundmass. The majority of the surrounding groundmass appears to be filled pore space, which is common for an altered volcanic breccia (Mordensky et al. 2018). In thin section 14 (Figure 10 right: altered andesite lava) no microfracturing is observed. The majority of the void space is composed of small, unfilled, connected pores in the matrix.

Table 5 provides the extent of alteration and microstructural description for each of the thin sections examined under the petrographic microscope and SEM, supplemented by descriptions from GNS Science reports (Rae et al. 2009; Rae et al. 2010; Siratovich et al. 2014) for samples 13, 4.2 and 21.4, which were not thin sectioned. The alteration is as described for comparable thin sections in the GNS Science reports (Rosenberg 1997; Milicich et al. 2008; Rae et al. 2009; Ramirez and Rae 2009; Rae et al. 2010; Sanders et al. 2015). For differentiation purposes, only sample sets with moderate-high or high alteration are labelled as 'altered' in the figures. We find that the samples do not show a systematic relationship between alteration extent and depth (Table 5).

Mechanical triaxial testing

Triaxial deformation experiments were performed on samples from sample sets 11 and 14 at effective pressures of 40 and 70 MPa. The stress–strain curves and porosity reduction curves as a function of axial strain are plotted in Figure 11a,b, respectively. We first note that all samples were brittle at the tested effective pressures: all samples contained macroscopic shear fractures following deformation, the hallmark of brittle deformation (see definitions in Wong and Baud 2012; Heap and Violay 2021). We find that the peak stress of sample sets 11 and 14 increased as the effective pressure was increased (Figure 11). For example, the peak stress at failure for sample set 14 increased from ~155 to ~180 MPa as effective pressure was increased from 40 to 70 MPa (Figure 11a). The axial strain required to reach the peak stress also increased for both sample sets as the effective pressure was increased (Figure 11a). For example, the axial strain required for the peak stress for sample set 11 increased from ~1.5 to ~2% as effective pressure was increased from 40 to 70 MPa (Figure 11a). We also highlight that, for both sample sets, an increase in effective pressure decreased the slope of the strain softening portion of the stress–strain curves (i.e. the stress drop); this is most evident in sample set 11 (Figure 11a). The porosity reduction curves show that the samples first compacted followed by dilation, apart from the sample from sample set 14 deformed at 70 MPa, which compacted throughout (Figure 11b).

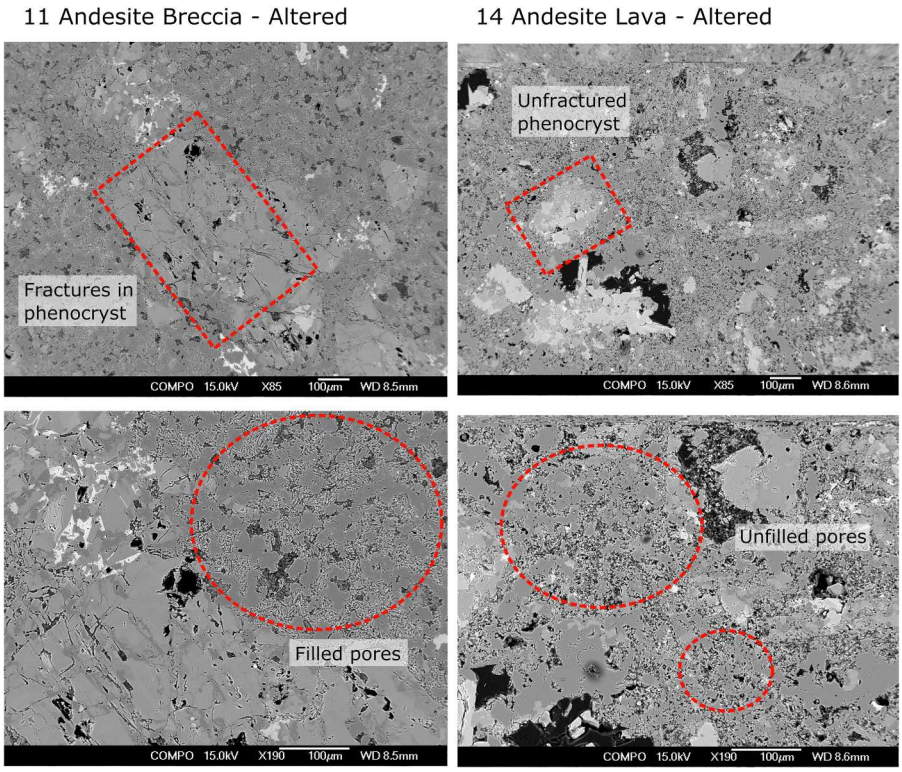

Figure 10. SEM images highlighting the microstructure contrast between sample sets 11 (left) and 14 (right). Features of interest are labelled on each panel.

Table 5. Alteration extent from thin section interpretation and key textural observations from SEM images, augmented by descriptions from GNS reports.

Sample set	Depth (m)	Alteration extent	Textural observations from thin section and SEM interpretation
16 Rhyolite breccia	501	Moderate Angular breccia clasts replaced by clays.	Phenocrysts show jig saw style fractures. Presence of pumice described for this unit in RK9 (Rosenberg 1997).
1 Rhyolite lava	905	Very weak Plagioclase phenocrysts are fresh, with traces of calcite and illite in microfractures; pyroxene and hornblende are completely altered to chlorite, calcite leucoxene and sphene; magnetite is fresh. (Rosenberg 1997).	Microfracture network within phenocrysts; dense groundmass surrounding phenocrysts.
15 Rhyolite pumice ignimbrite	1113	Weak-moderate Ash sized matrix and pumice clasts mostly replaced by clays, chlorite and oxides; plagioclase phenocrysts mostly unaltered.	'Partially welded, crystal-rich pumice ignimbrite' (Rae et al. 2010). Plagioclase and quartz phenocrysts highly fractured, surrounded by fine-grained pumice matrix.
3 Fine grained sandstone conglomerate	1511	None	Unaltered sandstone clasts (detrital quartz and plagioclase) in matrix of micaceous clay and chlorite (Rosenberg 1997).
7 Brecciated andesite	1821	Moderate-high Most groundmass and phenocrysts are replaced with secondary minerals. Plagioclase altered to albite, calcite, illite; pyroxenes altered to biotite-chlorite, epidote, calcite, anhydrite and actinolite; groundmass has quartz, chlorite, calcite and epidote replacement (Ramirez and Rae 2009).	Phenocrysts of plagioclase and pyroxene are fractured and surrounded by fine-grained groundmass, throughgoing fractures filled with epidote and chlorite (veins).
11 Andesite breccia	1852	High Groundmass pore space is variably filled by secondary minerals, such as quartz, chlorite, calcite, leucoxene and epidote, while plagioclase phenocrysts are partially altered to epidote, calcite quartz and albite and pyroxenes are completely altered to chlorite, epidote and leucoxene (Rae et al. 2009).	Phenocrysts show remnant highly fractured textures. Some of these fractures persist within the phenocrysts but do not propagate into the groundmass.
12 Andesite lava clast within a breccia	1854	High Most of the matrix and phenocrysts replaced by secondary quartz, leucoxene, chlorite, calcite and oxides Plagioclase is partially to completely altered to albite, epidote, calcite, fine grained quartz, pyroxenes are completed altered to chlorite, epidote and leucoxene (Rae et al. 2009).	Porphyritic andesite with 10-15% phenocrysts dominated by plagioclase, pyroxene and ilmenite, within an extremely fine-grained groundmass (Rae et al. 2009). Phenocrysts are not fractured.
14 Andesite lava	2081	Moderate-high Plagioclase completed altered to epidote, albite and chlorite; pyroxene completed altered to chlorite and epidote; ground mass altered to chlorite, epidote, quartz (Ramirez et al. 2009).	No microfractures observed; few phenocrysts, the majority of the pore space is unfilled and connected.
4.2 Andesite lava	2121	Weak-moderate Plagioclases fresh to slightly altered to andaluria, pyroxenes highly altered to chlorite (Siratovich et al. 2014).	Plagioclase phenocrysts show rare microfractures.
13 Andesite lava	2147	Weak Plagioclases are fresh, pyroxenes and groundmass have minor alteration.	Most pyroxenes and plagioclase phenocrysts fractured.
10 Andesite breccia	2200	High Plagioclase altered to epidote, chlorite and albite, pyroxenes completed altered to chlorite, epidote and titanite, matrix is altered to chlorite, epidote, titanite, albite, quartz and pyrite (Ramirez et al. 2008).	Microfractures through and around plagioclase and pyroxene phenocrysts; majority of the surrounding fine-grained groundmass contains filled pore space.
21.4 Andesite breccia	2320	Moderate-high Plagioclase partially to strongly altered to adularia, calcite and epidote, pyroxene completely altered to chlorite, epidote and calcite, magnetite completely altered to leucoxene and groundmass completely altered to hematite and quartz with calcite and chlorite (Rae et al. 2010).	Intergranular microfractures infilled as veins with quartz, epidote, biotite and calcite (Siratovich et al. 2014). Phenocrysts microfractured, partially crushed and fragmented (Rae et al. 2010).
6 Hydrothermally altered fine grained sandstone (Basement Greywacke)	2606	Weak-moderate Secondary mineralogy of clay, chlorite, leucoxene, pyrite, calcite and epidote; plagioclase altered to albite; minor iron oxide staining (Milicich et al. 2008).	Semi-metamorphosed clast-supported rock fabric composed of detrital quartz, altered felspars and indisctinct lithics (Milicich et al. 2008) in a fine groundmass with very few pores; fractures infilled (veins) with quartz.

We also note that the amount of compaction, and the strain at which the samples began to dilate, increased as the effective pressure was increased (Figure 11b). Following deformation, the porosities of all samples were reduced relative to their starting porosities (Figure 11b).

The triaxial experiments on sample sets 11 and 14 were conducted at effective confining pressures much higher than those in-situ and show that, if these rocks were buried deeper, samples 11_1, 11_2 and 14_2 would likely undergo initial compaction followed by dilational microcrack formation and

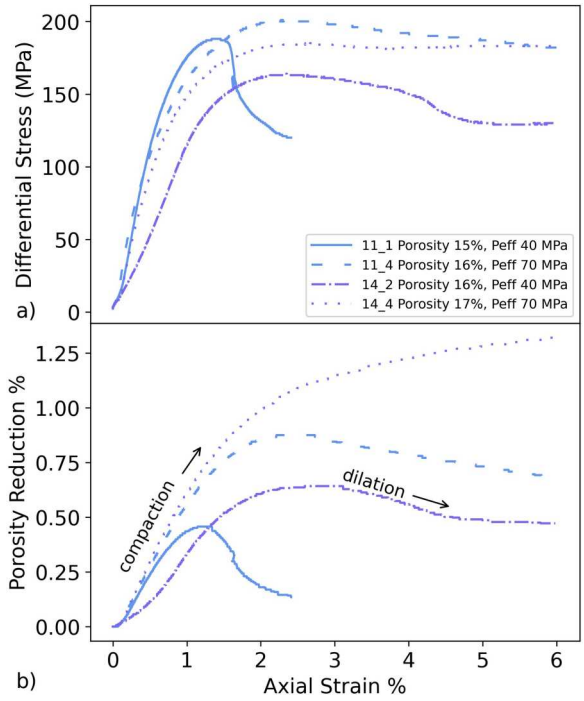

Figure 11. Differential stress (a) and porosity reduction (b) and as a function of axial strain for samples from sample sets 11 and 14 deformed under an effective pressure of 40 and 70 MPa; colour coded according to lithological description in Figure 5.

coalescence until failure (Figure 11). This is evident when visually inspecting the post-deformation samples, which display clear strain localisation (Figure 12). Sample 14_4 exhibits consistent compaction (Figure 11b), however it also eventually develops a localised failure surface (Figure 12). It is likely that, at slightly higher effective pressures, these rocks would transition from brittle to ductile behaviour.

Interpretation

One of the most important properties in a geothermal system is permeability. Matrix permeability (i.e. intact rock permeability) is controlled by the quantity and tortuosity of the void space within the rock. The quantity and tortuosity of this void space are a result of many factors, including the mode of formation and any subsequent geological processes occurring after formation (Cant et al. 2018). Geothermal environments, including the RGF, are typically situated in geochemically harsh, volcanically and tectonically active areas, creating highly altered, micro-structurally complex and spatially variable rocks. This highlights that while geological units may be grouped, significant variation exists within them.

Siratovich et al. (2014) showed that rocks of the Rotokawa Andesite contain a pervasive network of isotropic microcracks induced by thermal stress. Multiple geological episodes, including initial eruption, burial in a faulted graben, hydrothermal alteration and exhumation during core recovery, have caused the rocks to undergo multiple heating and cooling cycles (Rae 2007; Siratovich et al. 2014). Siratovich et al. (2014) also demonstrated the extent of microfracturing influenced the physical and mechanical properties of the rocks, such as ultrasonic wave velocities and uniaxial compressive strength. Here, physical property relationships are discussed, in particular how they relate to the matrix permeability. This is followed by a discussion of how these relationships can be of use to geothermal exploitation and other applications.

Physical properties

The relationships between the various physical and mechanical characteristics highlighted in the results show that for the sample sets from the Rotokawa reservoir, ultrasonic wave velocities could be used to estimate porosity or density, but not permeability. Dynamic modulus, a function of v_p, v_s and density, could also be used to predict porosity and

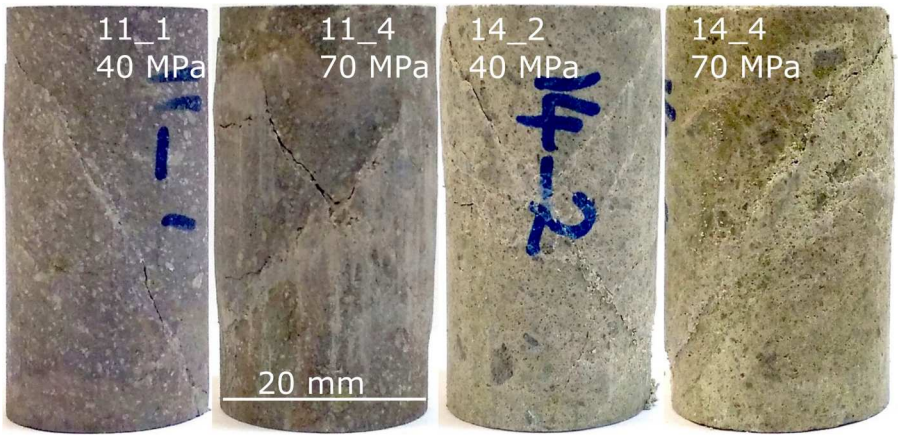

Figure 12. Photos of cores post triaxial deformation showing the resulting macroscopic shear fractures. We highlight that samples 11_4 and 14_4 (and to some degree sample 14_2), the samples deformed at the highest effective pressure, show some off-fault damage.

permeability. The relationships between porosity and density and permeability are also robust, as also observed by several authors (Bourbie and Zinszner 1985; Stimac et al. 2004; Siratovich et al. 2014; Farquharson et al. 2015; Cant et al. 2018).

Matrix permeability is not only controlled by the volume of the void space, but also by the morphology and tortuosity of the void space (Cant et al. 2018), resulting in the moderate data scatter in Figure 6a. An examination of the SEM images from thin sections 11 and 14 (Figure 10), which have similar porosity but permeability differing by nearly two orders of magnitude, highlights one of the sources of variation (Figure 6a). The microfracture network in sample 11 creates a narrow, tortuous path, which does not extend from the phenocrysts to the filled pores, resulting in a rock with a low-permeability that is highly sensitive to confinement. The connectivity of the porosity in sample 14 does not rely on narrow microfractures, resulting in a rock with a high permeability that is not particularly sensitive to confinement. We also highlight that the pore space in 14 is more evenly distributed than in 11, encouraging connectivity, further promoting the higher permeability.

Petrophysical depth profiles

Porosity, density, ultrasonic wave velocity and dynamic Young's modulus tend to systematically change with increasing depth from which the sample was obtained (Figure 13), as also shown by Massiot et al. (2022), although there is considerable spread in the data. Our porosity measurements were undertaken at ambient pressure. We would expect them to decrease with confinement, up to 3% (Durán et al. 2019; Eggertsson et al. 2020; Carbillet et al. 2021). This would be associated with a similarly small increase in density, an increase in ultrasonic wave velocity (up to 20% for pressures at 50 MPa (Durán et al. 2019)) and an increase in dynamic Young's modulus (28–100% for pressures at 50 MPa (Durán et al. 2019)). Therefore, the depth-related changes in these parameters observed for this dataset would be more pronounced if measured at in-situ pressures.

These depth-related variations at laboratory conditions highlight that burial and alteration processes have had a systematic, albeit variable, effect on the physical properties of the rocks in the Rotokawa geothermal reservoir. Certainly, compaction of the high-porosity volcanic and volcaniclastic rocks could be responsible for some of these changes, similar to compaction processes in sedimentary rocks. Alteration also has an effect, although these effects have been shown to be variable and secondary to the texture of the protolith (Mordensky et al. 2018; Durán et al. 2019).

A closer inspection of Figure 13 shows that the properties of the altered andesite breccias do not change with depth, and the altered andesite lavas have higher porosity than the slightly deeper non-altered andesite lavas. It is important to note that physical properties can change within a single flow unit, for example porosity of less than 5% for dense coherent andesite lava and greater than 25% for its brecciated margin, as observed by Mordensky et al. (2018). In addition, the presence of unaltered or

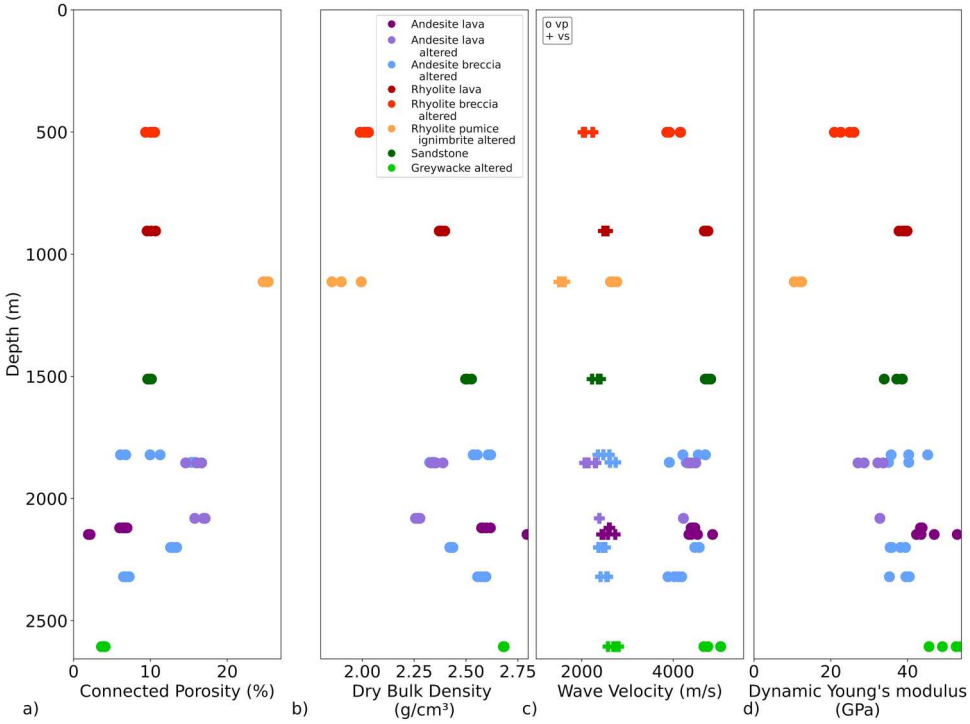

Figure 13. Depth profiles for ambient pressure a) porosity b) density, c) ultrasonic wave velocity and d) dynamic Young's modulus.

more porous or less dense material at greater depth than altered or less porous or denser material highlights that increased depth does not necessarily correspond to increased alteration, decreased porosity and increased density. Meanwhile, the ignimbrites have higher porosity than the shallower rhyolite lavas and breccias, which have similar porosity to the deeper sandstone. Clearly, primary texture continues to play a significant role on the physical properties of the studied rocks, even after deep burial. As a whole, the rhyolite lavas and breccias tend to have a higher porosity, and lower density, ultrasonic wave velocity and dynamic Young's modulus than the deeper andesite lavas and breccias. This highlights the complex interaction of burial, alteration grade (e.g. argillic versus propylitic), and original texture on the physical properties of the rocks in the TVZ, as also shown by Cant et al. (2018). This study provides additional data and interpretation of the properties of buried and altered volcanic rocks from geothermal systems to fill in some of the gaps remaining from Cant et al. (2018), while also confirming that systematic relationships are not evident in these environments. More studies on these materials are necessary to adequately characterise the highly variable subsurface.

Effect of confining pressure

Increasing the confining pressure acting on samples in a laboratory can be used as a proxy for increased depth. As observed in Figure 7, increasing confining pressure causes a decrease in permeability for most samples. It is shown in Cant et al. (2018) and (Durán et al. 2019), for example, that the type (rounded pores, microfractures, or a mix of both) of connected porosity plays a significant role as to how sensitive rocks are when pressure is applied. Cant et al. (2018) found that the permeability of volcanic samples with a porosity predominantly consisting of microfractures was much more sensitive to confining pressure, whereby a larger decrease in permeability was observed when confining pressure was applied than for samples with pore-dominated porosity.

This effect can be further demonstrated for this dataset by contrasting sample sets 11 and 14, which have similar porosity (16–17%) and density (2.33–2.27 g/cm^3). As summarised in Table 5, the microstructure of thin section 11 has a fracture network focussed in its phenocrysts and infilled pores, whereas thin section 14 exhibits unfilled porosity (Figure 10). The permeability of the pore-dominated sample set 14 does not decrease, even when 30 MPa is applied, whereas, the permeability of sample set 11, a sample that contains some fractures, progressively reduces its original permeability by 50% at 30 MPa confinement (Figure 7). The comparison between the mechanical behaviour of the sample sets 11 and 14 with that of fresh, unaltered volcanic rocks (for example from Heap and Violay 2021) suggests that the complex microstructure and alteration that characterises sample sets 11 and 14 has influenced their mechanical behaviour such that, when compared with fresh, unaltered volcanic rocks of a similar porosity, they will likely transition to ductile behaviour at lower effective pressures.

Because of their aspect ratio, microfractures initially close elastically at low pressures or differential stresses, with surface roughness and asperity height controlling further, non-elastic closure at higher stress (Cant et al. 2018; Durán et al. 2019). In contrast, the closure or collapse of round pores requires high pressures or differential stresses. Since both samples have similar moderate-high propylitic alteration (see Table 1) and porosity, this leaves the primary texture (breccia versus lava), pore size, the presence of pore infilling and microfractures as the main differences between the rock types, and presumably, results in the different observed mechanical behaviours. The infilled pores and crystal-limited microfractures in sample set 11 both reduce permeability and increase the strength, when contrasted to sample set 14, which contains unfilled pores.

Sample set 16 (altered rhyolite breccia from 501 m depth) exhibits the highest permeability sensitivity to confining pressure. The calculated in-situ stress for this shallowest sample is ~3.5 MPa. The confinement was only increased to 15 MPa for this sample set because applying a confining pressure above the maximum in-situ stress could cause non-recoverable deformation of the sample, resulting in permeability measurements that do not reflect the state of this material. The permeability decreased by nearly an order of magnitude over the tested range of confining pressures. Petrographic thin section analysis shows pervasive fractured phenocrysts (Figure 14), which are closed upon increasing the confining pressure, restricting fluid flow through the sample upon closure, again highlighting the role of microfractures on sensitivity of permeability to confining pressure.

In-situ permeability

A critical application of this dataset is to estimate in-situ permeability values. To determine an estimate of the in-situ permeability for each sample set, the dry density-based effective stress model was applied. Table 6 provides a summary of the calculated in-situ effective stress values from the stress model for each sample set, along with the calculated permeability value from the permeameter test run at the closest confining pressure. Figure 15 provides a permeability depth profile at the confining pressure closest to in-situ.

The permeability at the in-situ pressure shows a general decreasing trend; however, there is a wide

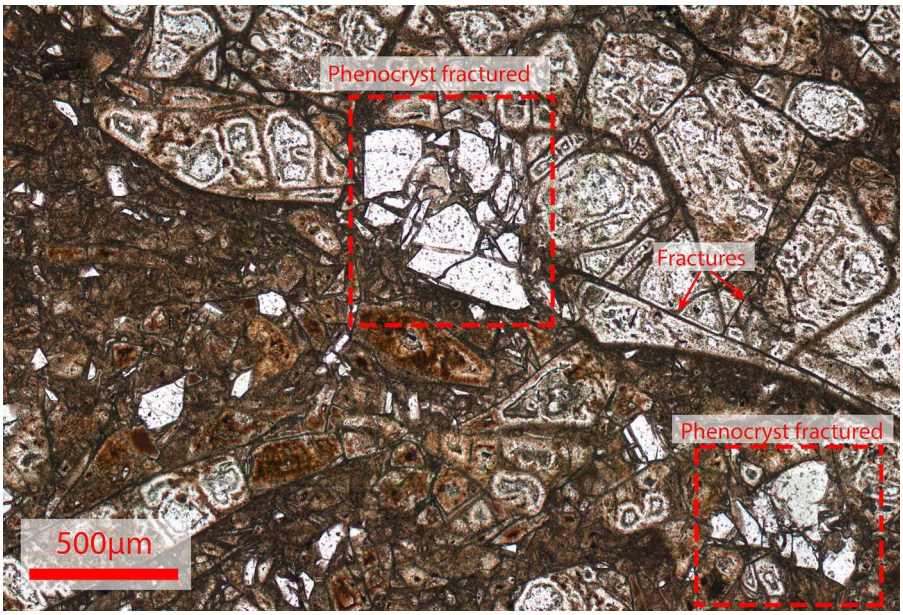

Figure 14. Plane polarised light photomicrograph for sample set 16 highlighting fracturing within the sample.

Table 6. In-situ confining stress calculated from the lithostatic model with the closest tested confining pressure and the corresponding permeability.

Sample set	Lithology	Depth (m)	Calculated in-situ effective vertical tress (MPa)	Tested confining pressure (MPa)	Permeability at/near calculated in-situ stress (m^2)
16_1	Rhyolite breccia	501	5	5	2.26E-18
16_3	Rhyolite breccia	501	5	5	2.67E-18
1_1	Rhyolite lava	905	12	12.5	1.09E-18
1_3	Rhyolite lava	905	12	12.5	1.24E-18
3_1	Sandstone conglomerate	1511	23	25	2.77E-19
3_3	Sandstone conglomerate	1511	23	25	2.22E-19
7_3	Andesite breccia altered	1821	30	30	1.15E-19
11_1	Andesite breccia altered	1852	25	25	3.43E-18
11_3	Andesite breccia altered	1852	25	25	4.23E-18
11_4	Andesite breccia altered	1852	25	25	4.20E-18
12_2	Andesite lava altered	1854	25	25	1.96E-18
12_3	Andesite lava altered	1854	25	25	1.53E-18
14_1	Andesite lava altered	2081	30	30	1.72E-16
14_2	Andesite lava altered	2081	30	30	2.36E-16
14_4	Andesite lava altered	2081	30	30	2.39E-16
27_4.2_1	Andesite lava	2120	32	30	1.91E-19
27_4.2_3	Andesite lava	2120	32	30	1.61E-19
10_1	Andesite breccia altered	2200	30	30	3.80E-18
10_3	Andesite breccia altered	2200	30	30	1.92E-18
30_21.4_4	Andesite breccia altered	2320	29	30	2.45E-19
30_21.4_6	Andesite breccia altered	2320	29	30	3.02E-19
6_1	Greywacke altered	2606	38	20	5.42E-20
6_3	Greywacke altered	2606	38	20	8.88E-20

range of permeabilities for the andesite lava and breccia (Table 6). This is once again related to the microstructure of each sample set, and how each rock responds differently to increased confining pressure, in particular for the Rotokawa Andesite, which varies laterally and vertically, and is the result of several eruptive flows (McNamara et al. 2015).

Application to geothermal exploration and exploitation

The purpose of conducting this research is to explore the ability to help predict hard to obtain parameters, such as permeability, for the exploitation of geothermal systems. The core used in this study was extremely

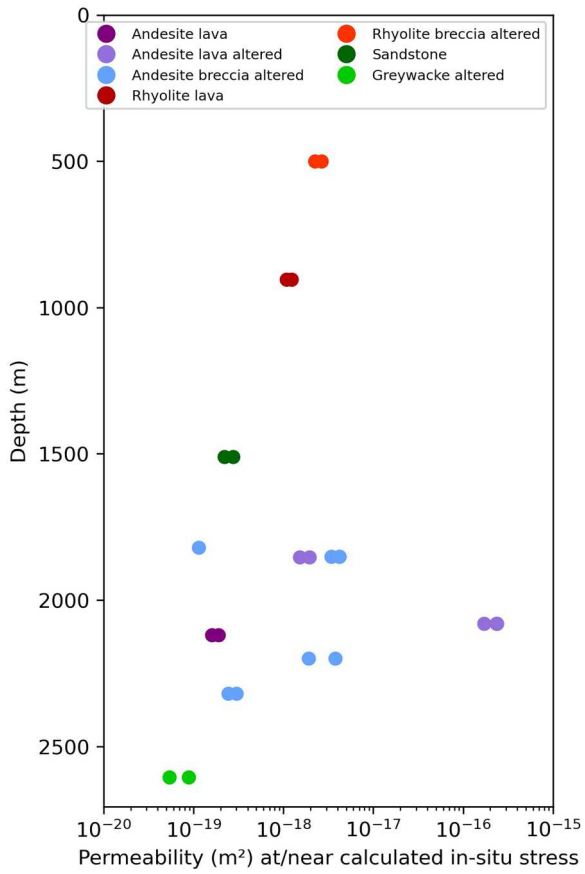

Figure 15. Depth profiles for permeability at the nearest confining pressure to the calculated in-situ effective stress.

expensive, time consuming and potentially risky to recover (Siratovich et al. 2014). There are downhole geophysical logging techniques for measuring porosity and ultrasonic wave velocity measurements (Massiot et al. 2022). With the use of the relationships described in this research, these measurements (in particular porosity, but also dynamic Young's modulus derived from ultrasonic wave velocities and density) can be used to predict values which are more difficult to obtain, such as matrix permeability, using the regression formulas provided in Figure 4. These relationships, however, do not account for macro-scale features, such as macrofractures, which will have an effect on both permeability (e.g. feed zones, as described in McNamara et al. (2015) and (Massiot et al. 2017)) and the geophysical measurements themselves. Additional work is needed to link downhole measurements, as in Massiot et al. (2022) and laboratory measurements, such as those presented here.

It must be emphasised that these predictions are only estimates. The scatter of data, caused by the heterogeneous nature of the rocks, results in a range of behaviour and properties at given depths and lithologies. A prime example of this is the similarities and differences between sample sets 11 (breccia) and 14 (lava) from the Rotokawa Andesite unit. Another example is the very poor fit of ultrasonic wave velocities with permeability. The Rotokawa Andesite is grouped based on a geochemical signature (McNamara et al. 2015), and not on physical and mechanical properties. From a rock mechanics perspective, the variability in the mechanical relationships described in this research demonstrate the importance of thorough investigation of localised samples, especially when hosted in a hydrothermally active system.

This research also provides depth profiles for several physical properties in the RGF. While the models show a systematic trend with depth, the cause of this relationship is manifold and complex. Nevertheless, these profiles can provide first-order estimates for a variety of properties representing a wide range of stratigraphic units present in the RGF. Siratovich et al. (2014) fitted microstructural and empirical correlations which took into account micro-structural variances in the model. The use of the data in this research could be used to further refine these models.

Conclusions

The objective of this research was to carry out a systematic laboratory study of the physical and mechanical properties of the Rotokawa geothermal field using a unique sample set from core obtained during well drilling, and relate them to in-situ stress conditions, as well as to each other. The following are key conclusions of the research:

- While there is a general relationship between porosity and permeability, the effect of microstructure can cause significant variation permeability, so correlation may be used taking into account a variability within half an order of magnitude.
- The complex microstructure and alteration of samples from the Rotokawa geothermal field reduces their strength and the pressure at which they transition to ductile behaviour, when compared with mechanical data for fresh, unaltered volcanic rocks from the literature. Differences in the mechanical behaviour of the tested samples varies as a result of their different microstructures (primary texture, pore size, presence of microfractures), owing to their similar alteration grade and intensity. The large variations in microstructure observed within the Rotokawa geothermal field suggests a wide range of mechanical properties and behaviour.
- Bench-top ultrasonic wave velocities have minimal correlation with permeability; however, when combined with density to calculate the dynamic Young's modulus, a power-law fit could be used to estimate permeability. A number of linear and power-law fits were also derived for various physical parameters, which could be used for estimating difficult to obtain parameters.
- There is a general trend of decreasing permeability with increasing confining pressure. The presence of

microfractures results in a permeability sensitive to confining pressure. Samples with no microfractures and unfilled pores show little to no decrease in permeability with confining pressure as long as the confining pressure is lower than the in-situ stress.
- Despite an overall trend with depth, there is a wide range in porosity, density, ultrasonic wave velocity, dynamic Young's modulus and permeability that depends on both the original and altered microstructural textures of individual samples.

Acknowledgements

The authors acknowledge Mercury NZ Ltd. and Tauhara North #2 Trust for providing the core used for experiments and access to the GNS Science Consultancy Reports used in this research.

Disclosure statement

No potential conflict of interest was reported by the author(s).

Funding

This work was supported by Mercury NZ Ltd.; funding for T. Jones was provided by Callaghan Innovation through their R&D Student Fellowship Grant fund (New Zealand Ministry of Business, Innovation and Employment under grant number: MRPR1401/PROP-41284-RDFELLOW-MRPOWER); the Dumont d'Urville NZ-France Science & Technology Support Programme from the New Zealand Royal Society Te Apārangi; the Interdisciplinary Thematic Institute (ITI) GeoT, part of the 2021–2028 ITI program of the University of Strasbourg, the French National Research Centre (CNRS) and the French National Institute of Health and Medical Research (Inserm). The ITI GeoT was supported by the SFRI-STRAT'US project, under grant number ANR-20-SFRI-0012, and by IdEx Unistra, under the grant number ANR-10-IDEX-0002, within the Investments for the Future (PIA) framework. M. J. Heap also acknowledges support from the Institut Universitaire de France (IUF).

Data availability statement

The data that support the findings of this study are openly available in the Zenodo repository at https://doi.org/10.5281/zenodo.12633937. The data consist of excel spreadsheets containing the raw measurement data as well as a pdf containing representative photomicrographs of all samples.

ORCID

Marlène C. Villeneuve http://orcid.org/0000-0001-6001-0786

References

Bibby H, Caldwell T, Davey F, Webb T. 1995. Geophysical evidence on the structure of the Taupo Volcanic Zone and its hydrothermal circulation. J Volcanol Geotherm Res. 68(1–3):29–58. doi:10.1016/0377-0273(95)00007-H

Bourbie T, Zinszner B. 1985. Hydraulic and acoustic properties as a function of porosity in Fontainebleau Sandstone. J Geophys Res: Solid Earth. 90(B13):11524–11532. doi:10.1029/JB090iB13p11524.

Brown SJ, Wilson CJN, Cole JW, Wooden J. 1998. The Whakamaru group ignimbrites, Taupo Volcanic Zone, New Zealand: evidence for reverse tapping of a zoned silicic magmatic system. J Volcanol Geotherm Res. 84 (1–2):1–37. doi:10.1016/S0377-0273(98)00020-1.

Cant JL, Siratovich PA, Cole JW, Villeneuve MC, Kennedy BM. 2018. Matrix permeability of reservoir rocks, Ngatamariki geothermal field, Taupo Volcanic Zone, New Zealand. Geotherm Energy. 6(1):2. doi:10.1186/s40517-017-0088-6.

Carbillet L, Heap MJ, Baud P, Wadsworth FB, Reuschlé T. 2021. Mechanical compaction of crustal analogs made of sintered glass beads: the influence of porosity and grain size. J Geophys Res Solid Earth. 126(4). doi:10.1029/2020JB021321.

Cole J, Deering C, Burt R, Sewell S, Shane P, Matthews N. 2014. Okataina Volcanic Centre, Taupo Volcanic Zone, New Zealand: a review of volcanism and 65 synchronous pluton development in an active, dominantly silicic caldera system. Earth-Sci Rev. 128:1–17. doi:10.1016/j.earscirev.2013.10.008.

Colombier M, Wadsworth FB, Gurioli L, Scheu B, Kueppers U, Muro AD, Dingwell DB. 2017. The evolution of pore connectivity in volcanic rocks. Earth Planet Sci Lett. 462:99–109. doi:10.1016/j.epsl.2017.01.011.

Davidson J, Siratovich P, Wallis I, Gravley D, McNamara D. 2012. Quantifying the stress distribution at the Rotokawa geothermal field, New Zealand. In: New Zealand Geothermal Workshop 2012 Proceedings 19–21 November 2012 Auckland, New Zealand.

Durán EL, Adam L, Wallis IC, Barnhoorn A. 2019. Mineral alteration and fracture influence on the elastic properties of volcaniclastic rocks. J Geophys Res Solid Earth. 124 (5):4576–4600. doi:10.1029/2018JB016617.

Eggertsson GH, Kendrick JE, Weaver J, Wallace PA, Utley JEP, Bedford JD, Allen MJ, Markússon SH, Worden RH, Faulkner DR, et al. 2020. Compaction of hyaloclastite from the active geothermal system at Krafla Volcano, Iceland. Geofluids. 2020:1–17. doi:10.1155/2020/3878503.

Farquharson J, Heap MJ, Varley NR, Baud P, Reuschlé T. 2015. Permeability and porosity relationships of edifice-forming andesites: A combined field and laboratory study. J Volcanol Geoth Res. 297:52–68. doi:10.1016/j.jvolgeores.2015.03.016.

Farquharson JI, Baud P, Heap MJ. 2017. Inelastic compaction and permeability evolution in volcanic rock. Solid Earth. 8(2):561–581. doi:10.5194/se-8-561-2017.

Fortin J, Stanchits S, Vinciguerra S, Guéguen Y. 2011. Influence of thermal and mechanical cracks on permeability and elastic wave velocities in a basalt from Mt. Etna volcano subjected to elevated pressure. Tectonophysics. 503(1–2):60–74. doi:10.1016/j.tecto.2010.09.028.

Heap M, Kennedy B. 2016. Exploring the scale-dependent permeability of fractured andesite. Earth Planet Sci Lett. 447:139–150. doi:10.1016/j.epsl.2016.05.004.

Heap MJ, Gravley DM, Kennedy BM, Gilg AH, Bertolett E, Barker S. 2020. Quantifying the role of hydrothermal alteration in creating geothermal and epithermal mineral resources: the Ohakuri ignimbrite (Taupō Volcanic Zone. New Zealand). J Volcanol Geotherm Res. 390:106703. doi:10.1016/j.jvolgeores.2019.106703.

Heap MJ, Lavallée Y, Petrakova L, Baud P, Reuschlé T, Varley NR, Dingwell DB. 2014. Microstructural controls on the physical and mechanical properties of edifice-forming andesites at Volcán de Colima, Mexico. J Geophys Res Solid Earth. 119(4):2925–2963. doi:10.1002/2013JB010521.

Heap MJ, Meyer GG, Noël C, Wadsworth FB, Baud P, Violay MES. 2022. The permeability of porous volcanic rock through the brittle-ductile transition. J Geophys Res Solid Earth. 127(6). doi:10.1029/2022jb024600.

Heap MJ, Violay MES. 2021. The mechanical behaviour and failure modes of volcanic rocks: a review. Bull Volcanol. 83(5). doi:10.1007/s00445-021-01447-2.

Hochstein M. 1995. Crustal heat transfer in the Taupo Volcanic Zone (New Zealand): comparison with other volcanic arcs and explanatory heat source models. J Volcanol Geotherm Res. 68:117–151. doi:10.1016/0377-0273(95)00010-R.

Houghton BF, Wilson CJN, McWilliams MO, Lanphere MA, Weaver SD, Briggs RM, Pringle MS. 1995. Chronology and dynamics of a large silicic magmatic system: central Taupo Volcanic Zone. Geology. 23(1):13. doi:10.1130/0091-7613(1995)023<0013:CADOAL>2.3.CO;2

Kanakiya S, Adam L, Rowe MC, Esteban L, Lerner GA, Lindsay JM. 2022. Petrophysical and elastic properties of altered lavas from Mt. Taranaki: implications for dome stability. J Volcanol Geotherm Res. 432:107693. doi:10.1016/j.jvolgeores.2022.107693.

Kereszturi G, Heap M, Schaefer LN, Darmawan H, Deegan FM, Kennedy B, Komorowski J-C, Mead S, Rosas-Carbajal M, Ryan A, et al. 2023. Porosity, strength, and alteration – Towards a new volcano stability assessment tool using VNIR-SWIR reflectance spectroscopy. Earth Planet Sci Lett. 602:117929. doi:10.1016/j.epsl.2022.117929.

Massiot C, McIntosh I, Deans J, Milicich SD, Tontini FC, Ronde Cd, Adam L, Kolandaivelu K, Guerin G. 2022. Petrophysical facies and inferences on permeability at brothers volcano, Kermadec arc, using downhole images and petrophysical data. Econ Geol. doi:10.5382/econgeo.4897.

Massiot C, Nicol A, McNamara DD, Townend J. 2017. Evidence for tectonic, lithologic, and thermal controls on fracture system geometries in an andesitic high-temperature geothermal field. J Geophys Res Solid Earth. 122(8):6853–6874. doi:10.1002/2017JB014121.

McNamara D, Sewell S, Buscarlet E, Wallis IC. 2016. A review of the Rotokawa Geothermal Field, New Zealand. Geothermics. 59(Part B):281. doi:10.1016/j.geothermics.2015.07.007.

McNamara DD, Massiot C, Lewis B, Wallis IC. 2015. Heterogeneity of structure and stress in the Rotokawa Geothermal Field, New Zealand. J Geophys Res Solid Earth. 120(2):1243–1262. doi:10.1002/2014JB011480.

Milicich SD, Chambefort I, Wilson CJN, Alcaraz S, Ireland TR, Bardsley C, Simpson MP. 2020. A zircon U-Pb geochronology for the Rotokawa geothermal system, New Zealand, with implications for Taupō Volcanic Zone evolution. J Volcanol Geotherm Res. 389:106729. doi:10.1016/j.jvolgeores.2019.106729.

Milicich SD, Rosenberg MD, Bignall G. 2008. Geology of injection well RK20, Rotokawa Geothermal Field. Technical Report February, GNS Science, Lower Hutt, New Zealand.

Montanaro C, Ray L, Cronin SJ, Calibugan A, Rott S, Bardsley C, Scheu B. 2023. Linking top and subsoil types, alteration and degassing processes at Rotokawa geothermal field, New Zealand. Front Earth Sci. 10:1067012. doi:10.3389/feart.2022.1067012.

Mordensky SP, Villeneuve MC, Kennedy BM, Heap MJ, Gravley DM, Farquharson JI, Reuschlé T. 2018. Physical and mechanical property relationships of a shallow intrusion and volcanic host rock, Pinnacle Ridge, Mt. Ruapehu, New Zealand. J Volcanol Geoth Res. 359:1–20. doi:10.1016/j.jvolgeores.2018.05.020.

Nara Y, Meredith PG, Yoneda T, Kaneko K. 2011. Influence of macro-fractures and micro-fractures on permeability and elastic wave velocities in basalt at elevated pressure. Tectonophysics. 503(1–2):52–59. doi:10.1016/j.tecto.2010.09.027.

Oetomo AB. 2015. OEtomo_2015.pdf. In: 15th Indonesian Scholars International ConventionLondon, 3–4 October 2015. London.

Palmer AS. 1982. Kawakawa Tephra in Wairarapa, New Zealand, and its use for correlating Ohakea loess. N Zealand J Geol Geophys. 25(3):305–315. doi:10.1080/00288306.1982.10421494.

Rae A. 2007. Rotokawa geology and geophysics. GNS Science consultancy report 2007/83.

Rae AJ, McCoy-West A, Ramirez LE. 2009. Geology of production wells RK26 and RK27, Rotokawa Geothermal Field. GNS Science Consultancy Report 2009/10.

Rae AJ, McCoy-West A, Ramirez LE, McNamara D. 2010. Geology of production wells RK30L1 and RK30L2 Rotokawa Geothermal Field. GNS Science Consultancy Report 2010/02.

Ramirez LE, Milicich SD, Bignall G, Rae AJ. 2008. Geology of injection well RK25, Rotokawa geothermal field GNS Science Consultancy Report 2008/332.

Ramirez LE, Rae AJ. 2009. Geology of injection well RK24/RK24ST1 Rotokawa geothermal field. GNS Science Consultancy Report 2009/04.

Ramirez LE, Rae AJ, McCoy-West AJ, Alcaraz S. 2009. Geology of production well RK29, Rotokawa Geothermal Field GNS Science Consultancy Report 2009/305.

Rosenberg W. 1997. Geology of production well RK9 and reinjection well RK12: Rotokawa geothermal field. GNS Science Consultancy Report 1997.

Rossetti L, Healy D, Hole M, Petroleum M-J. 2019. Evaluating petrophysical properties of volcano-sedimentary sequences: A case study in the Paraná-Etendeka Large Igneous Province. Mar Petrol Geol. 102:638–656. doi:10.1016/j.marpetgeo.2019.01.028.

Rowland JV, Sibson RH. 2001. Extensional fault kinematics within the Taupo Volcanic Zone, New Zealand, soft linked segmentation of a continental rift system. N Z J Geol Geophys. 44(22):271–283. doi:10.1080/00288306.2001.9514938.

Sanders F, Simpson MP, Chambefort I. 2015. Geology of well RK34 and RK34-ST1, Rotokawa geothermal field. GNS Science Consultancy Report 2015/03.

Schaefer LN, Kereszturi G, Kennedy BM, Villeneuve M. 2023. Characterizing lithological, weathering, and hydrothermal alteration influences on volcanic rock properties via spectroscopy and laboratory testing: a case study of Mount Ruapehu volcano. N Zeal Bull Volcanol. 85(8):43. doi:10.1007/s00445-023-01657-w.

Sibson RH, Rowland JV. 2003. Stress, fluid pressure and structural permeability in seismogenic crust, North Island, New Zealand. Geophys J Intern. 154(2):584–594. doi:10.1046/j.1365-246X.2003.01965.x.

Siratovich PA, Aulock Fv, Lavallée Y, Cole JW, Kennedy BM, Villeneuve MC. 2015. Thermoelastic properties of

the Rotokawa Andesite: A geothermal reservoir constraint. J Volcanol Geotherm Res. 301:1–13. doi:10.1016/j.jvolgeores.2015.05.003.

Siratovich PA, Heap MJ, Villeneuve MC, Cole JW, Kennedy BM, Davidson J, Reuschlé T. 2016. Mechanical behaviour of the Rotokawa Andesites (New Zealand): insight into permeability evolution and stress-induced behaviour in an actively utilised geothermal reservoir. Geothermics. 64:163–179. doi:10.1016/j.geothermics.2016.05.005.

Siratovich PA, Heap MJ, Villenueve MC, Cole JW, Reuschlé T. 2014. Physical property relationships of the Rotokawa Andesite, a significant geothermal reservoir rock in the Taupo Volcanic Zone, New Zealand. Geotherm Energy. 2(1):10. doi:10.1186/s40517-014-0010-4.

Stimac JA, Powell TS, Golla GU. 2004. Porosity and permeability of the Tiwi geothermal field, Philippines, based on continuous and spot core measurements. Geothermics. 33(1–2):87–107. doi:10.1016/j.geothermics.2003.03.002.

Ulusay R, Hudson J. 2007. The complete ISRM suggested methods for rock characterization, testing and monitoring: 1974–2006. Antalya, Turkey: Elsevier.

Vinciguerra S, Trovato C, Meredith PG, Benson PM. 2005. Relating seismic velocities, thermal cracking and permeability in Mt. Etna and Iceland basalts. Int J Rock Mech Min Sci. 42(7–8):900–910. doi:10.1016/j.ijrmms.2005.05.022.

White SP, Mroczek EK. 1998. Permeability changes during the evolution of a geothermal field due to the dissolution and precipitation of quartz. Transp Porous Media. 33(1–2):81–101. doi:10.1023/A:1006541526010.

Wohletz K, Heiken G. 1992. Volcanology and geothermal energy. Los Angeles: University of California Press.

Wong T, Baud P. 2012. The brittle-ductile transition in porous rock: A review. J Struct Geol. 44:25–53. doi:10.1016/j.jsg.2012.07.010.

Wyering L, Villeneuve M, Wallis I, Siratovich P, Kennedy B, Gravley D, Cant J. 2014. Mechanical and physical properties of hydrothermally altered rocks, Taupo Volcanic Zone, New Zealand. J Volcanol Geotherm Res. 288:76–93. doi:10.1016/j.jvolgeores.2014.10.008.

Zhu Z, Tian H, Jiang G, Dou B. 2022. Effects of high temperature on rock bulk density. Géoméch Geoeng. 17(2):647–657. doi:10.1080/17486025.2020.1827169.